Available online at www.sciencedirect.com
SCIENCE DIRECT®
Theoretical and Applied Fracture Mechanics 39 (2003) 23–45
theoretical and applied fracture mechanics
www.elsevier.com/locate/tafmec

Numerical, experimental, nondestructive, and image analyses of damage progression in cast A356 aluminum notch tensile bars

M.F. Horstemeyer [a,*], Ken Gall [a], K.W. Dolan [b], A. Waters [b], J.J. Haskins [b], D.E. Perkins [b], A.M. Gokhale [c], M.D. Dighe [c]

[a] *Center for Materials and Engineering Sciences, Sandia National Laboratories, Solid and Material Mechanics Department, Livermore, CA 94550, USA*
[b] *Lawrence Livermore National Laboratory, Livermore, CA 94550, USA*
[c] *Materials Science and Engineering Department, Georgia Institute of Technology, Atlanta, GA 30332, USA*

Abstract

Void nucleation, growth, and coalescence in A356 aluminum notch specimens was determined from a combination of experiments, finite element analysis, nondestructive analysis, and image analysis. Notch Bridgman tension experiments were performed on specimens to failure and then other specimens were tested to 90%, 95%, and 98% of the failure load. The specimens were evaluated with nondestructive X-ray tomography and optical image analysis. Finite element simulations of the notch tests were performed with an elastic–plastic internal state variable material model that incorporated the pertinent microstructures (silicon particle volume fraction and size distribution and porosity volume fraction and size distribution). Parametric finite element simulations were performed to give insight into various initial conditions and responses of the notch tensile bars. The various methods all corroborated the same damage progression.

1. Introduction

In recent years there has been a strong research initiative by the automotive industry to improve the performance of cast aluminum components. Among other things, one critical aspect of optimizing design is to better understand and quantify damage evolution in cast aluminum under monotonic loads. Developing the ability to predict damage progression is imperative for the design of components that will experience overloads during service due to impacts and rough ground. The progression of damage in nearly all ductile materials subjected to monotonic loading is due to the nucleation, growth, and coalescence of voids [1]. In metallic alloys, the nucleation and subsequent growth of voids occurs primarily at second phase inclusions or precipitates [2–5]. Due to their

* Corresponding author. Tel.: +1-925-294-2816; fax: +1-925-294-1459.
E-mail address: mfhorst@sandia.gov (M.F. Horstemeyer).

0167-8442/03/$ - see front matter © 2003 Elsevier Science Ltd. All rights reserved.
PII: S0167-8442(02)00136-2

heterogeneous microstructure, cast aluminum alloys are particularly vulnerable to void-crack nucleation, growth and coalescence from Si, Mg, and Fe particles. In addition, cast aluminum alloys contain voids (porosity) due to local feeding obstruction through dendritic solidification fronts, trapped gases, or temperature gradient driven solidification shrinkage [6,7]. Notably, pores can exist at different material length scales ranging from the submicron size to several hundred microns, depending on the solidification process. The size, shape and distribution of the pores will have a strong influence on damage evolution, localization, and mechanical properties of aluminum castings [7–9].

The microstructure of hypoeutectic cast A356 Al consists of the main (Al–1.6wt.%Si) and eutectic (Al–12.6wt.%Si) phases. In the eutectic regions, large silicon particles and clusters form a dendritic substructure while the Si remains solutionized in the main phase. The microstructural alterations have a strong influence on the monotonic mechanical properties of Al castings through changes in void nucleation, growth, and coalescence characteristics. Under monotonic loads, cast aluminum alloys with a smaller DAS or spheroidized Si particles generally demonstrate more macroscopic ductility and greater ultimate tensile strengths [8,10–15].

With this background, it is clear that the monotonic mechanical properties of cast aluminum alloys are controlled by the multiscale mechanisms of void nucleation, growth and coalescence from Si particles and preexisting pores. Numerous studies have been performed to understand damage progression in different metallic alloys [16–39]. However, previous experimental studies have not examined the progression of void nucleation, growth, and coalescence with the combined complementary analyses of continuum damage mechanics, X-ray tomography, and optical methods. To fully exploit the current metallurgical findings and precisely predict the deformation and damage progression of cast aluminum, a link between modeling predictions and experimental results should be firmly established. This work aims to establish such a link through the methods that will be described next.

The present work includes a comparative study of experimental data, numerical finite element simulations, optical microscopy and stereology, and X-ray computed tomography (CT) of notch tensile tests in a cast A356 aluminum alloy. Notch Bridgman tensile specimens were monotonically loaded to different strain levels up to and including failure. The notch geometry was used to create stress triaxiality gradients in the specimen to validate the experimental and numerical methods. After mechanical testing, the damage in the specimens was determined using a CT method. CT is a nondestructive testing technique that uses X-rays to accurately determine the local density changes. For the optical image analysis, the specimens were sectioned and metallographically prepared. Optical microscopy coupled with digital image analysis techniques was used to obtain high precision pictures of the pertinent surface, which provided a benchmark comparison tool for the CT technique. The CT method determines three-dimensional porosity distributions, while the sectioning method only provides information for a representative two-dimensional cross-section. However, the two-dimensional cross-section technique represents the most widespread method for determining the evolution of many microstructural parameters such as casting porosity [40]. The finite element analysis included the use of the large deformation temperature and rate dependent, internal state variable (ISV) plasticity model [41,42] hereafter. The plasticity model [41,42] has also been modified for void nucleation, growth and coalescence [37,43]. The constants for the plasticity and damage model were calibrated to experimental stress–strain results for tension, compression, torsion, tension-followed-by-compression, and compression-followed-by-tension [43]. The material model is implemented into the ABAQUS implicit finite element code using a mesh that has identical dimensions as the Bridgman tensile specimens. This numerical analysis allows the prediction of spatial damage progression as a function of the applied load.

Succeeding sections of this paper present the cast material information, experimental techniques, numerical modeling method, and a discussion of the results, and conclusions.

2. Cast material and mechanical testing

The composition of the A356 Al alloy is; 7% Si, 0.4% Mg, 0.01% Fe, 0.01% Cu, 0.01% Mn, 0.01% Sr, 0.01% Ti, 0.01% Zn, and balance aluminum. To produce A356 cast plates, an A356.2 ingot was melted in an induction furnace. The melt was grain refined with titanium–boron, was strontium modified, and degassed using a rotary degasser. The castings were poured between 950 and 977 K, and then fully cooled over a 16-h period. The A356 aluminum plates were cast in rectangular molds with interior dimensions of $25 \times 14 \times 5$ cm. Iron chills were employed on the top, bottom, and end of the casting mold to simulate a permanent mold casting. A no-bake silica sand was used to create the sides of the plate, the riser, and the down sprue. A ceramic foam filter was used between the down sprue and the riser. The plates were removed from the mold and given a T6 anneal (solutionized at 810 K for 16 h, quenched in hot water at 344 K, and then aged for 4 h at 518 K). This produced an average dendrite cell size of approximately 25 μm.

Mechanical test specimens were cut from a cast plate orthogonal to the solidification direction in order to assure that different initial porosity levels with homogeneously distributed pores would result within the specimens. A variation in the initial conditions of the test samples provided an additional dimension to evaluate the performance of the damage characterization and prediction techniques. The different levels of initial porosity in the specimens were helpful in determining if the driving force for ductile damage depended more on the material characteristics (pore size, volume fraction, and distribution) or the applied boundary conditions. For wrought alloys, the damage progresses mainly in the center of the specimen due to the high stress triaxiality [41,44]. The specimen notch radius was 2.97 mm, with a notch root diameter of 9.23 mm and a shoulder diameter of 12.7 mm. The gage radius was 4.7625 mm. Hence, the ratio of gage radius to notch size, which reflects the stress triaxiality, is 1.6, a moderate triaxiality. The displacements were measured using an extensometer with a 25.4 mm gage length placed across the notch. Cross-sectional views of the samples are provided on several of the visual

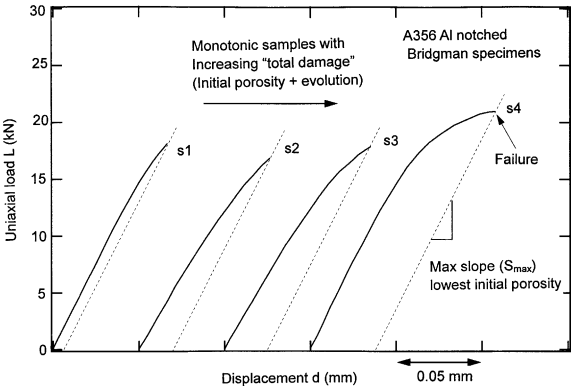

Fig. 1. Load–displacement curves for notched cast A356 Al specimens. The displacement was measured across the notch using an extensometer with a 25.4 mm gage length. The area between the maximum observed effective elastic stiffness, S_{max}, and the curve is a relative measurement of total specimen damage.

damage images. All specimens were loaded at an approximate strain rate of 10^{-4} s^{-1} at room temperature.

The load–displacement responses of the four different cast A356 Al specimens are shown in Fig. 1. The Bridgman specimen numbers S1, S2, and S3 were unloaded prior to failure at 90%, 95%, and 98% of the failure load on the curves in Fig. 1. The failure load was determined by specimen S4.

The percentage of failure load varies depending on the initial porosity level. For example, S2 had a higher initial porosity level than S4 as shown by the optical images in Fig. 2. The initial total porosity level for these two specimens were measured in material extracted adjacent to the notch region before testing. The initial porosity level for S2 was 0.02 and for S4 was 0.0009. When comparing these two, the 95% load level is not precise because the failure load for S2 was smaller than S4. However, by monitoring the loads instead of displacements to determine the prefailure point, we retrieved a more reliable result. When trying to control with displacements, premature failure of the specimen would result because of the variability in the initial porosity level and distribution. Because increased porosity degrades the effective elastic modulus, S2 and S3 have larger initial porosity levels as evident from microstructural data and the smaller effective elastic stiffness observed in these curves.

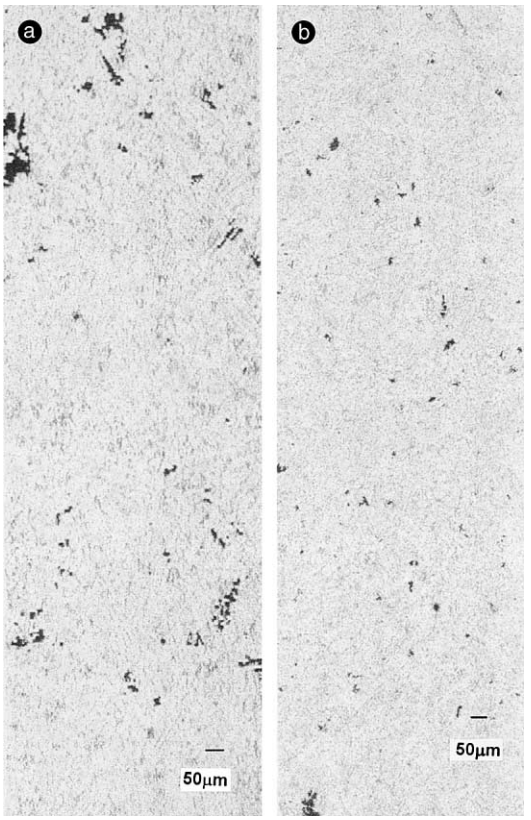

Fig. 2. Optical images of two different specimens (a) S2 and (b) S4 showing the variation of initial porosity from specimen to specimen.

The maximum effective elastic stiffness among the four specimens, S_{max}, can be used in part to estimate the relative difference in total damage between the Bridgman specimens. The value of S_{max} represents the "elastic" response of the Bridgman specimen with the lowest initial porosity level. As shown in Fig. 1 by the dashed lines, the unloading of all specimens is assumed to occur along S_{max}. With this construction, the area between the actual load–displacement response and the idealized unloading curve is a relative measure of the initial porosity superposed with the subsequent damage (plasticity) in the specimens. For example, in Fig. 1 specimen S1 is brought to a higher load level than specimen S2. However, the total damage in specimen S2 is larger (greater area between the S_{max} line and the load–displacement curve) due to its increased initial porosity. Using the area criterion, the curves in Fig. 1 are arranged in order of ascending total damage. The developed trend in total specimen damage is consistent with nondestructive and metallographic damage measurements that will be discussed later.

3. Computed tomography

CT produces two- and three-dimensional spatial data convolved with a fourth dimension that is the X-ray linear attenuation coefficient. The linear attenuation coefficient (LAT) is a function of material density, elemental composition, and X-ray energy. For specimens that have homogeneous elemental composition, changes in the LAT represent changes in material density. For inhomogeneous samples, changes in the LAT represent either density changes or segregation of elemental consituents, or both. Voids in the material result in LAT values of zero or near zero depending on spatial resolution.

Volumetric data is produced by first obtaining two-dimensional X-ray transmission images (projections) for a systematic set of specimen rotations. CT reconstruction software converts the two-dimensional projections into a complete volumetric representation of the object. This volumetric data can be sectioned in any two-dimensional planes to provide arbitrary cross-sectional planes (tomograms) of the specimen. The tomograms, coupled with volumetric image rendering techniques, accurately depict internal structures, geometries, and density/elemental variations within the specimen. Discontinuities such as gas holes and shrinkage porosity are well defined in the CT image, depending on the system resolution and discontinuity size. When individual pores in a local region are smaller than the system resolution, that region will appear to have a lower density than the surrounding nonporous material.

Two system parameters of importance for image interpretation are contrast sensitivity and spatial resolution. Contrast sensitivity is the ability of the CT system to detect variations in thickness and/or density. Spatial resolution is the ability of the system to resolve small features or details. The CT system can detect density variations as small as 0.1%, and

provide this information as a function of spatial location in the object. Spatial resolution depends on system design, sampling plan, and image reconstruction method. The detector element size and projection magnification together with sampling plan (i.e., number of projection angles) determine both pixel size for two-dimensional slice images and voxel (volume element) size for three-dimensional images. For the experimental setup employed here, the pixel (voxel) dimension was 28 μm. Structural features smaller than approximately two pixel (voxel) dimensions are not resolved, rather they lead to a lower average density measurement. Deconvolution of image blur using a measured point spread function is accomplished before CT reconstruction to produce sharper (higher contrast and resolution) reconstructed images.

The CT data acquisition system used in the present study is an area-array (two-dimensional) third-generation (rotation only) system. It consists of a 450 kV constant potential X-ray machine source with a 1.0 mm focal spot, and a detector system that uses a thermoelectrically cooled CCD camera (14-bit, 1024×1024 pixels) optically coupled to a high-density glass scintillator plate ($100 \times 100 \times 6$ mm) by a photographic lens. The mechanical staging for the system consists of three degrees of freedom: rotational, and x- and y-translation. These are driven by a computer-controlled system that provides movement in all three axes. Data preprocessing, image reconstruction, and analysis are typically done on a high level workstation. The system was configured with a projection magnification of nearly 1.0, and source-to-detector distance of 3000 mm. All data were acquired at 80 kV peak energy over a range of 180° with 1° scanning increments. Prior to reconstruction the images were preprocessed to subtract the camera dark current, correct for the source and detector variations correct for point-spread function and convert the raw data to CT number (i.e. linear attenuation coefficient). Ring removal and beam hardening were also performed in preprocessing.

For the four notch tensile specimens, the CT data were preprocessed to create segmented volumes ($460 \times 460 \times 400$). The voxels were designated in binary form with values of 1 and 0 for dense and void material. Voids less than 100 voxels (cubic pixels) are considered to be in the noise of experimental scatter. The number of voids greater than 100 voxels in size (0.002195 mm^3) per volume was calculated for each of the four samples. The results are presented in Table 1. Sample 4a and 4b designate both sides of the fractured sample S4.

Although the measurements in relation to a voxel are a volume, we can approximate a size by assuming that one side of the cubic voxel represents the void diameter. With this approximation, we can plot the void size versus frequency (binned according to size) for the four samples as shown in Fig. 3.

Here, the linear dimension of the voxel was 28 μm, and the voxel size is a volume ($0.028^3 \times 100$ mm^3). Fig. 4 shows the same data as a probability distribution function. This form of the data clearly shows that the largest void increases with progressing deformation (from S1 to S4). Note though that the largest size in sample S4 is less than the largest size in S3. This occurs because S4 fractured and the largest void would actually be the length of the fracture surface, which was not included.

4. Optical metallography

For optical microscopy, the specimens were sectioned along a central vertical plane in the loading direction and were metallographically prepared using standard techniques [40]. To quantify variations in the volume fraction of voids (void volume fraction is equal to the statistical

Table 1
Summary of results from X-ray tomography evaluations

	Sample 1	Sample 2	Sample 3	Sample 4a	Sample 4b
# void greater than 0.002195 mm^3	143	483	434	83	138
Volume of total material (mm^3)	1146.19	1140.5	1136.82	1333.56	1261.86

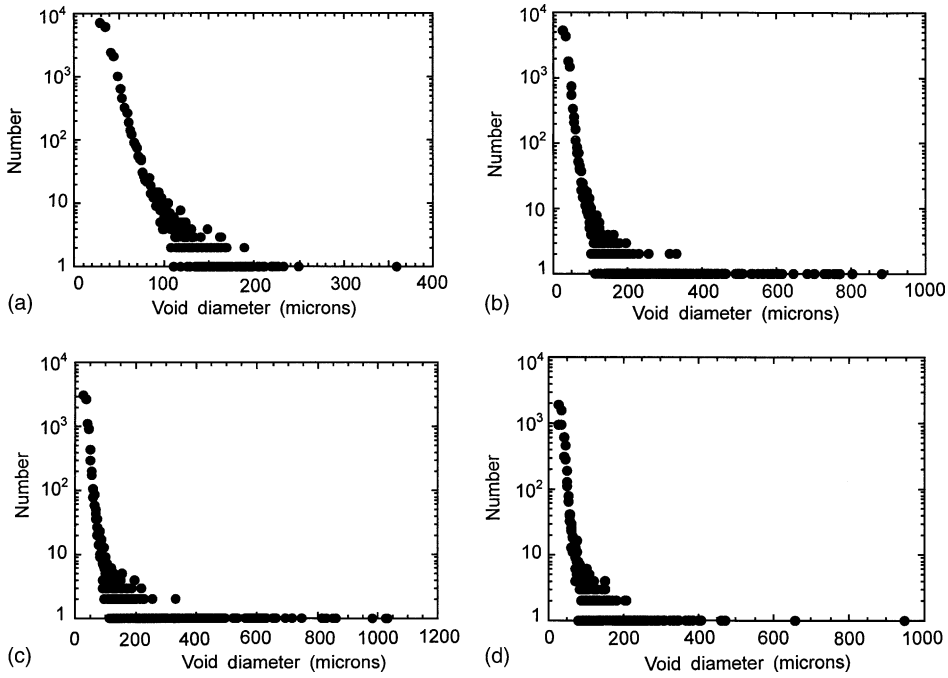

Fig. 3. X-ray tomography results showing the size distributions for the four samples: (a) S1, (b) S2, (c) S3, and (d) S4.

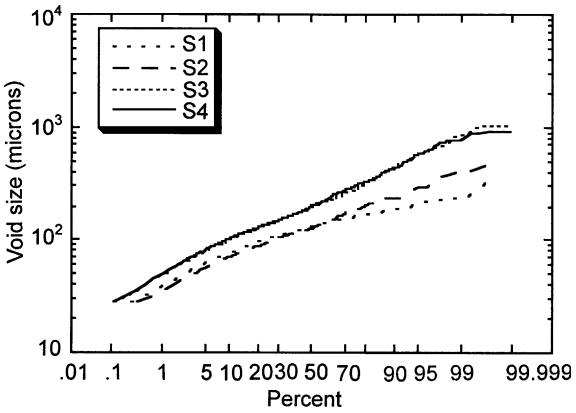

Fig. 4. Probability distribution function of four samples illustrating the varying void size as the deformation progressively increases from S1 through S4.

expected value of area fraction in a metallographic plane) as a function of radial and axial distance in the notch specimen, many measurements are made. Typically, only a few random individual frames are examined to obtain mean values, because homogeneous microstructures are assumed to be present. However, to capture a large region such as desired for these notch specimens, measurements must be performed on high-resolution images captured at sufficiently high magnification. The area of the observed microstructural field of view is inversely proportional to the square of the magnification, and therefore, at a high magnification only a very small region of the metallographic plane is observed in one field of view. To observe a large area of the metallographic plane at high resolution (high magnification) a digital image processing based technique [40,45–47] was used to create a large area image "montage" from contiguous microstructural fields digitally grabbed at high magnification. The procedure is equivalent to "cutting, matching, and pasting" a large number of high magnification contiguous microstructural frames; the borders of individual microstructural fields are matched to within one pixel precision.

5. Numerical modeling

Finite element analyses were performed of notch tensile specimens employing the modified

BCJ plasticity-damage model [43] in order to assess random variation versus homogeneous distribution of porosity within material. These types of analyses are useful to show which is more important: the mechanical response arising from the boundary conditions or from the material microstructure morphology. Quarter "plate" axisymmetric analyses using the finite element code ABAQUS were performed to study the effects of void nucleation, growth, and coalescence.

The equations used within the context of the finite element method are the rate of change of the observable and ISVs given by,

$$\overset{\circ}{\underline{\sigma}} = \dot{\underline{\sigma}} - \underline{W}^e\underline{\sigma} - \underline{\sigma}\underline{W}^e = \lambda(1-D)\,\mathrm{tr}(\underline{D}^e)\underline{I} + 2\mu(1-D)\underline{D}^e - \frac{\dot{D}}{1-D}\underline{\sigma}, \tag{1}$$

$$\underline{D}^e = \underline{D} - \underline{D}^{\mathrm{in}}, \tag{2}$$

$$\underline{D}^{\mathrm{in}} = f(T)\sinh\left[\frac{\|\underline{\sigma}'-\underline{\alpha}\| - \{R+Y(T)\}\{1-D\}}{V(T)\{1-D\}}\right]\frac{\underline{\sigma}'-\underline{\alpha}}{\|\underline{\sigma}'-\underline{\alpha}\|}, \tag{3}$$

$$\overset{\circ}{\underline{\alpha}} = \dot{\underline{\alpha}} - \underline{W}^e\underline{\alpha} + \underline{\alpha}\underline{W}^e = h(T)\underline{D}^{\mathrm{in}} - \left[\sqrt{\frac{2}{3}}r_{\mathrm{d}}(T)\|\underline{D}^{\mathrm{in}}\| + r_{\mathrm{s}}(T)\right]\|\underline{\alpha}\|\underline{\alpha}, \tag{4}$$

$$\dot{R} = H(T)\underline{D}^{\mathrm{in}} - \left[\sqrt{\frac{2}{3}}R_{\mathrm{d}}(T)\|\underline{D}^{\mathrm{in}}\| + R_{\mathrm{s}}(T)\right]R^2, \tag{5}$$

$$\dot{D} = [\dot{\phi}_{\mathrm{particles}} + \dot{\phi}_{\mathrm{pores}}]c + [\phi_{\mathrm{particles}} + \phi_{\mathrm{pores}}]\dot{c}, \tag{6}$$

$$\dot{\phi}_{\mathrm{particles}} = \dot{\eta}v + \eta\dot{v}, \tag{7}$$

$$\dot{\eta} = \|\underline{D}^{\mathrm{in}}\|\frac{d^{1/2}}{K_{\mathrm{IC}}f^{1/3}}\eta\left\{a\left[\frac{4}{27} - \frac{J_3^2}{J_2^3}\right] + b\frac{J_3}{J_2^{3/2}} + c\left\|\frac{I_1}{\sqrt{J_2}}\right\|\right\}, \tag{8}$$

$$\dot{v} = \frac{3}{2}v\left[\frac{3}{2}\frac{V(T)}{Y(T)}\frac{\sigma_H}{\sigma_{vm}} + \left(1 - \frac{V(T)}{Y(T)}\right)(1+0.4319)\right]^{Y(T)/V(T)}\underline{D}^{\mathrm{in}}, \tag{9}$$

$$\dot{c} = C_{\mathrm{coal}}[\eta\dot{v} + \dot{\eta}v], \tag{10}$$

$$\dot{\phi}_{\mathrm{pores}} = \left[\frac{1}{(1-\phi_{\mathrm{pores}})^m} - (1-\phi_{\mathrm{pores}})\right] \times \sinh\left\{\frac{2(2^{V(T)}/Y(T)^{-1})}{(2^{V(T)}/Y(T)^{+1})}\frac{\sigma_H}{\sigma_{vm}}\right\}\|\underline{D}^{\mathrm{in}}\|. \tag{11}$$

The rate equations are generally written as objective rates ($\overset{\circ}{\underline{\sigma}}, \overset{\circ}{\underline{\alpha}}$) with indifference to the continuum frame of reference assuming a Jaumann rate in which the continuum spin equals the elastic spin ($\underline{W} = \underline{W}^e$). The ISV equations (4)–(11) are functions of the observable variables (temperature, stress state, and rate of deformation). In general, the rate equations of generalized displacements, or thermodynamics fluxes, describing the rate of change may be written as independent equations for each ISV or as derivatives of a suitably chosen potential function arising from the hypothesis of generalized normality [48]. An advantage of assuming generalized normality, although somewhat restrictive, is unconditional satisfaction of the Kelvin inequality of the second law of thermodynamics (nonnegative intrinsic dissipation), i.e.

$$\underline{\sigma} : \underline{D}^{\mathrm{in}} - \underline{b} : \overset{\circ}{\underline{\alpha}} - \kappa \bullet \dot{R} - \phi \bullet \dot{D} \geqslant 0. \tag{12}$$

The selection of the ISVs may, in principle, be somewhat arbitrary, but the anisotropic hardening, isotropic hardening, and damage rate equations are physically motivated and strongly influence the history of the material. The BCJ ISV model accounts for deviatoric inelastic deformation resulting from the presence of dislocations in crystallographic materials, dilatational deformation, and ensuing failure from damage progression. Damage will reduce the material strength, enhance the inelastic flow, and soften the elastic moduli.

In Eq. (1), the elastic Lame constants are denoted by λ and μ. The elastic rate of deformation ($\underline{D}^e$) results when the total deformation ($\underline{D}$), which is defined by the boundary conditions, is subtracted from the flow rule as shown in Eq. (2). These second rank tensors are not to be confused with the scalar quantity of damage, D.

The independent variables for the inelastic rate of deformation are given in Eq. (3) as the stress, temperature, and IVSs. The deviatoric inelastic flow rule, $\underline{D}^{\text{in}}$, encompasses the regimes of creep and plasticity and is a function of the temperature, the anisotropic hardening ISV ($\underline{\alpha}$), the isotropic hardening ISV (R), the volume fraction of damaged material (D), and the functions $f(T)$, $V(T)$, and $Y(T)$, which are related to yielding with Arrhenius-type temperature dependence. The function $Y(T)$ is the rate-independent yield stress. The function $f(T)$ determines when the rate-dependence affects initial yielding. The function $V(T)$ determines the magnitude of rate dependence on yielding. These functions are determined from simple isothermal compression, tension, and torsion tests with different strain rates and temperatures,

$$\begin{aligned} V(T) &= C_1 \exp(-C_2/T), \\ Y(T) &= C_3 \exp(C_4/T), \\ f(T) &= C_5 \exp(-C_6/T). \end{aligned} \tag{13}$$

The anisotropic hardening ISV, $\underline{\alpha}$, reflects the effect of anisotropic dislocation density, and the isotropic hardening ISV R, reflects the effect of the global dislocation density. As such, the hardening equations (4) and (5) are cast in a hardening-recovery format that includes dynamic and static recovery. The functions $r_{\text{s}}(T)$ and $R_{\text{s}}(T)$ are scalar in nature and describe the diffusion-controlled static or thermal recovery, while $r_{\text{d}}(T)$ and $R_{\text{d}}(T)$ are scalar functions describing dynamic recovery. Hence, the two main types of recovery that are exhibited by populations of dislocations within crystallographic materials are captured in the ISVs. The anisotropic hardening modulus is $h(T)$, and the isotropic hardening modulus is $H(T)$.

The hardening moduli and dynamic recovery functions account for deformation-induced anisotropy arising from texture and dislocation substructures by means of stress-dependent variables. Using J_3^* in the hardening equations [49] the different hardening rates between axisymmetric compression and torsion (torsional softening) were accurately captured. This feature was included [50,51] in the BCJ ISV models as

$$r_{\text{d}}(T) = C_7\left(1 + C_{19}\left[\frac{4}{27} - \frac{J_3^{*2}}{J_2^{*3}}\right]\right)\exp(-C_8/T), \tag{14}$$

$$h(T) = \left\{C_9\left(1 + C_{20}\left[\frac{4}{27} - \frac{J_3'^2}{J_2'^3}\right]\right)\right\} - C_{10}T, \tag{15}$$

$$r_{\text{s}}(T) = C_{11}\exp(-C_{12}/T), \tag{16}$$

$$R_{\text{d}}(T) = C_{13}\left(1 + C_{21}\left[\frac{4}{27} - \frac{J_3^{*2}}{J_2^{*3}}\right]\right)\exp(-C_{14}/T), \tag{17}$$

$$H = \left\{C_{15}\left(1 + C_{22}\left[\frac{4}{27} - \frac{J_3'^2}{J_2'^3}\right]\right)\right\} - C_{16}T, \tag{18}$$

$$R_{\text{s}}(T) = C_{17}\exp(-C_{18}/T), \tag{19}$$

where $J_2' = \frac{1}{2}(\underline{\sigma}' - \underline{\alpha})^2$ and $J_3' = \frac{1}{3}(\underline{\sigma}' - \underline{\alpha})^3$. The deviatoric stress $\underline{\sigma}'$ is expressed in indicial notation as

$$\sigma_{ij}' = \sigma_{ij} - \tfrac{1}{3}\sigma_{ii}. \tag{20}$$

The damage variable D represents the damage fraction of material within a continuum element. The mechanical properties of a material depend upon the amount and type of microdefects within its structure. Deformation changes these microdefects, and when the number of microdefects accumulates, damage is said to have grown. The notion of a damaged state in continuum field theory emerged when a damage variable was introduced [52] to describe the microdefect density locally in an inelastic material. This notion was furthered [53] with a rate equation of void density. Examples of unified-creep-plasticity formulations were used [54,55] successfully for practical engineering applications. The BCJ equations follow the general philosophy of unified-creep-plasticity coupled with damage. However, Eq. (6) introduces the void volume fraction (porosity) as damage very much different than that in [52,53]. By including damage, D, as an ISV, different forms of damage rules can easily be incorporated into the constitutive framework. Demonstrated in [41,42,56,57] are the applicability of the void growth rule [58] used as the damage rate equation in the BCJ model.

Other related works show under quasi-static and high strain rate conditions that the plasticity-damage framework has been experimentally validated for large deformation plasticity and damage under blast loadings [56], large scale systems level damage analysis of explosions on ductile steel [57], development of forming limit diagrams under quasi-static loads [59], and penetration mechanics [43].

The generalized thermodynamic force conjugate, ϕ, is often referred to as the energy release rate for elastic brittle materials and the J-integral for inelasticity. In essence, an increment of damage will have associated energy released per unit damage extension as new damaged area (or volume) is developed.

In Eqs. (6)–(11), the damage progression is divided into void nucleation and growth from silicon particles and from pores. Coalescence is introduced to reflect pore–pore interactions and silicon-pore interactions as expressed in Eq. (10). The void nucleation evolution described by Eq. (8) is discussed in length [37]. The void growth related to silicon particles, Eq. (9), is that from [60]. Other forms can be used and evaluated [38], but this equation allows for a strain rate sensitivity in relation to the plasticity model ($m = V(T)/Y(T)$). For the porosity evolution, the [58] void growth rule [58] is used as shown in Eq. (11).

The combination of the plasticity and damage equations are solved simultaneously since the damage and stress equations are coupled. A nonlinear regression algorithm is used to determine material constants that are included in Appendix A. Since void nucleation occurs at a different rate under tension, compression, and torsion, a corresponding effect on the stress state arises. Discussed in [37] is the stress-state dependence of the void nucleation model. Before analysis of the notch tensile tests is performed, we determined the plasticity and damage constants for the material model with other (nonnotch) tests under tension, compression, torsion, tension-followed-by-compression, and compression-followed-by-tension. Fig. 5 shows a stress–strain comparison of the model (material constants are given in Appendix A) and uniaxial experiments under tension, compression, and torsion performed at room temperature and at

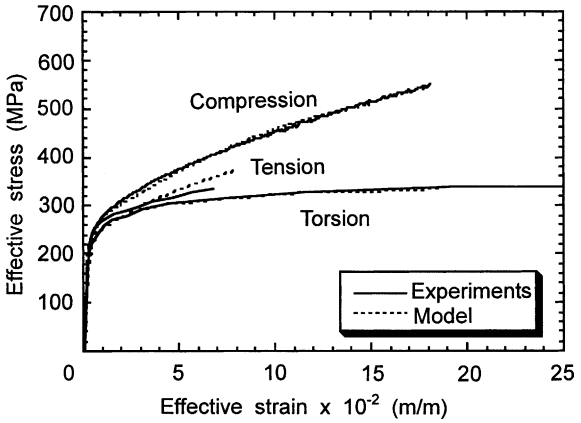

Fig. 5. Uniaxial stress–strain response comparing the plasticity-damage model and experiments for cast A356 aluminum under tension, compression, and torsion.

a strain rate of 10^{-4} s^{-1}. Fig. 6 shows a comparison of the void nucleation density versus effective strain which correspond to the stress–strain responses in Fig. 5. Other tests with the applied strain rate varying from 0.0001 to 3500 s^{-1} and temperature varying from 222 to 400 K were used to help determine some of the constants. Described in [38] are the details for material constant determination as well as the numerical implementation of the model.

Once the model parameters were determined from compression, tension, torsion, tension-followed-by-compression, and compression-followed-by-tension tests, predictive comparisons to the

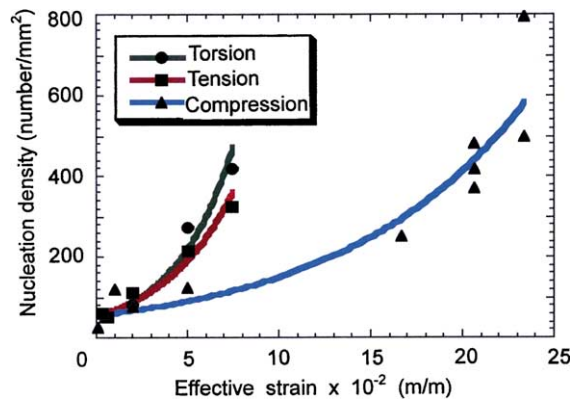

Fig. 6. Void nucleation response comparing the plasticity-damage model and experiments for cast A356 aluminum under tension, compression, and torsion.

notch tests could then be performed. Because variability in porosity levels and silicon particle distributions are evidenced in cast A356 aluminum structural components, the model was exercised with homogeneous and random distributions based on size. Moreover, included were different initial void volume fractions that could arise from different casting processes. Fig. 7 shows the load–displacement curves for the finite element simulations of notch tensile tests in which random and homogeneous initial porosity distributions were assumed with porosity levels of 0.0001 and 0.001. One observes from these simulations that the initially randomized porosity gives lower failure displacements than the homogeneous case. This difference lessens as the initial porosity level increases. It can be seen, from these initial assumptions that the failure displacements ranged from approximately 0.05–0.11 mm (the gage radius was 4.7625 mm). Later, we will show that the experimental failure displacement was approximately 0.11 mm indicating that our initial porosity assumptions were comparable to the experimental specimens.

Fig. 8 illustrates that the point of failure can occur at different locations and applied "strain" levels with different initial porosity levels and distributions. This is much different than a wrought alloy which fails at the notch center. The notch geometry generates stress and strain gradients from the specimen center to the notch edge. The highest stress triaxiality is at the specimen center, but the highest strain level occurs at the notch edge. This affects the void growth much differently depending upon the initial void distribution and porosity level. Fig. 9 shows the progression of total damage for the case with a random initial porosity level of 0.001.

In the case of initial homogeneous porosity distribution two cases arise. When the initial void volume fraction is 0.0001, the first element failure location occurs near the notch edge. This happens

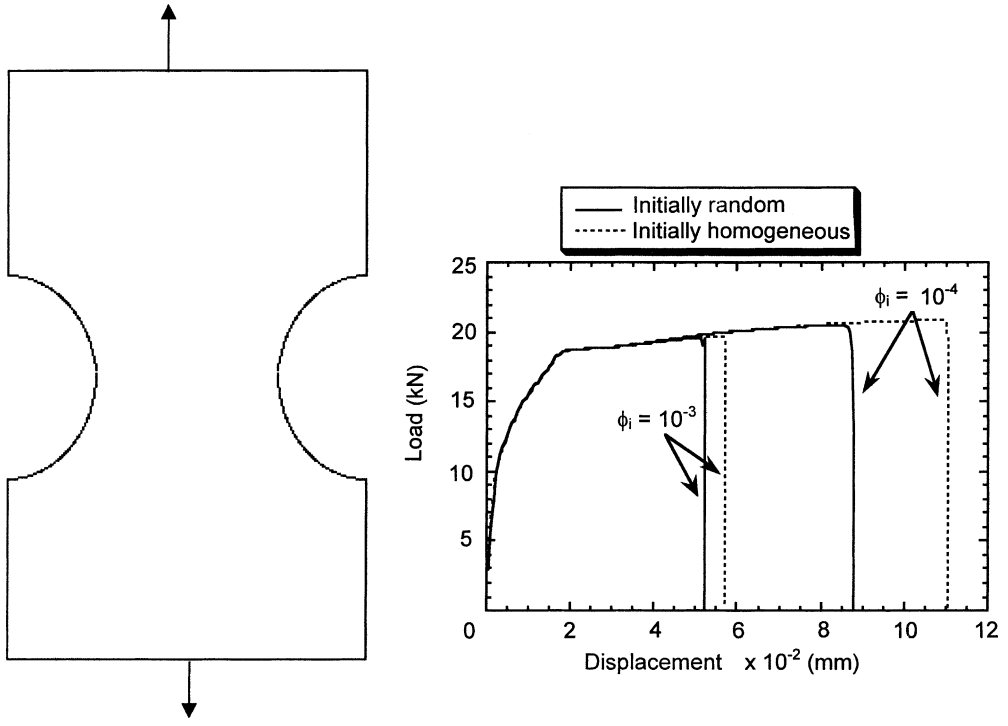

Fig. 7. Finite element simulations of load–displacement curves with four different initial assumptions for the microstructure: (a) initially homogeneous casting porosity with a level of 0.0001, (b) initially homogeneous casting porosity with a level of 0.001, (c) initially random casting porosity with a level of 0.0001, and (d) initially random casting porosity with a level of 0.001.

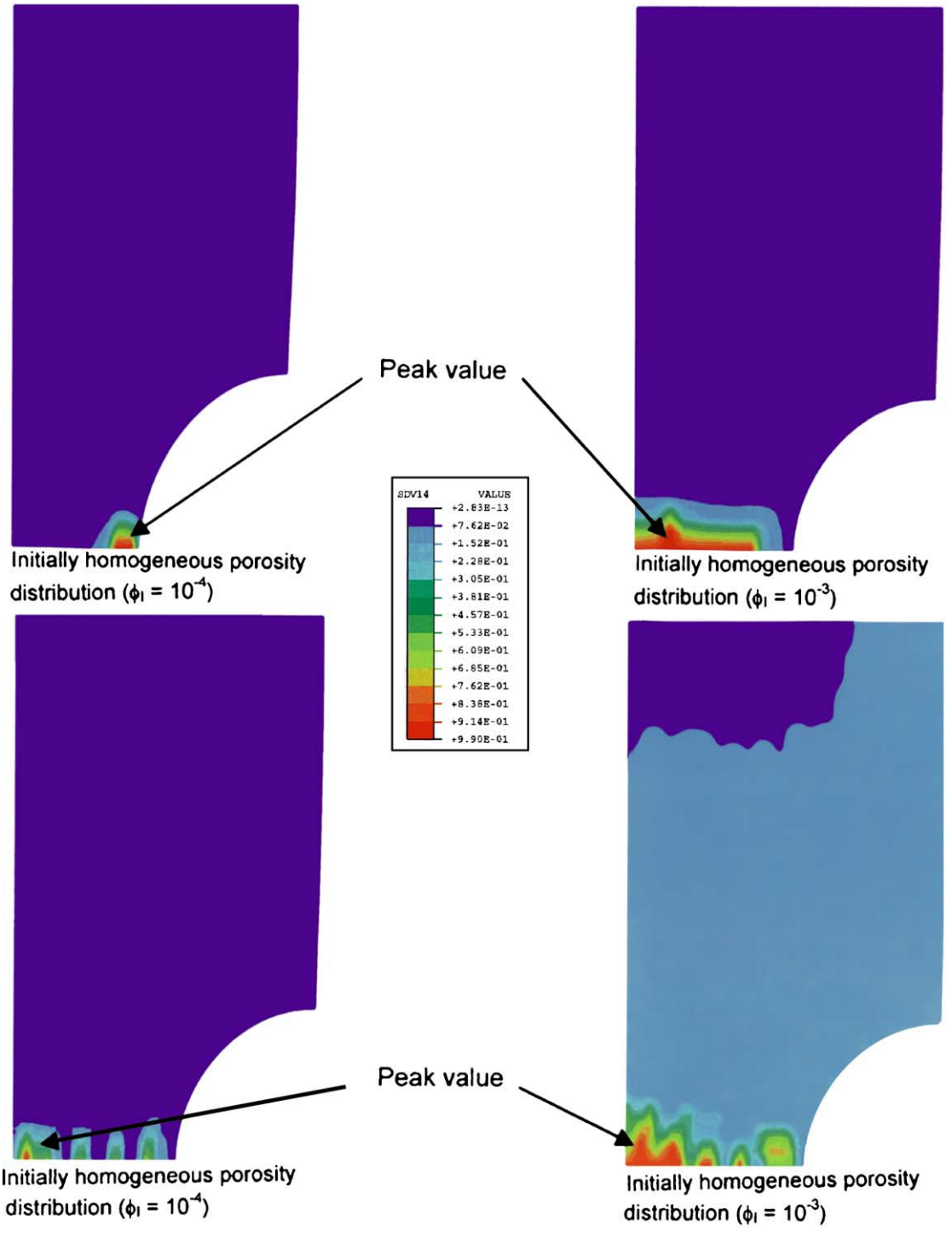

Fig. 8. Contour plots of total void volume fraction comparing the finite element simulations at first element failure, total damage (f) is SDV14, assuming initial random and homogeneous distributions.

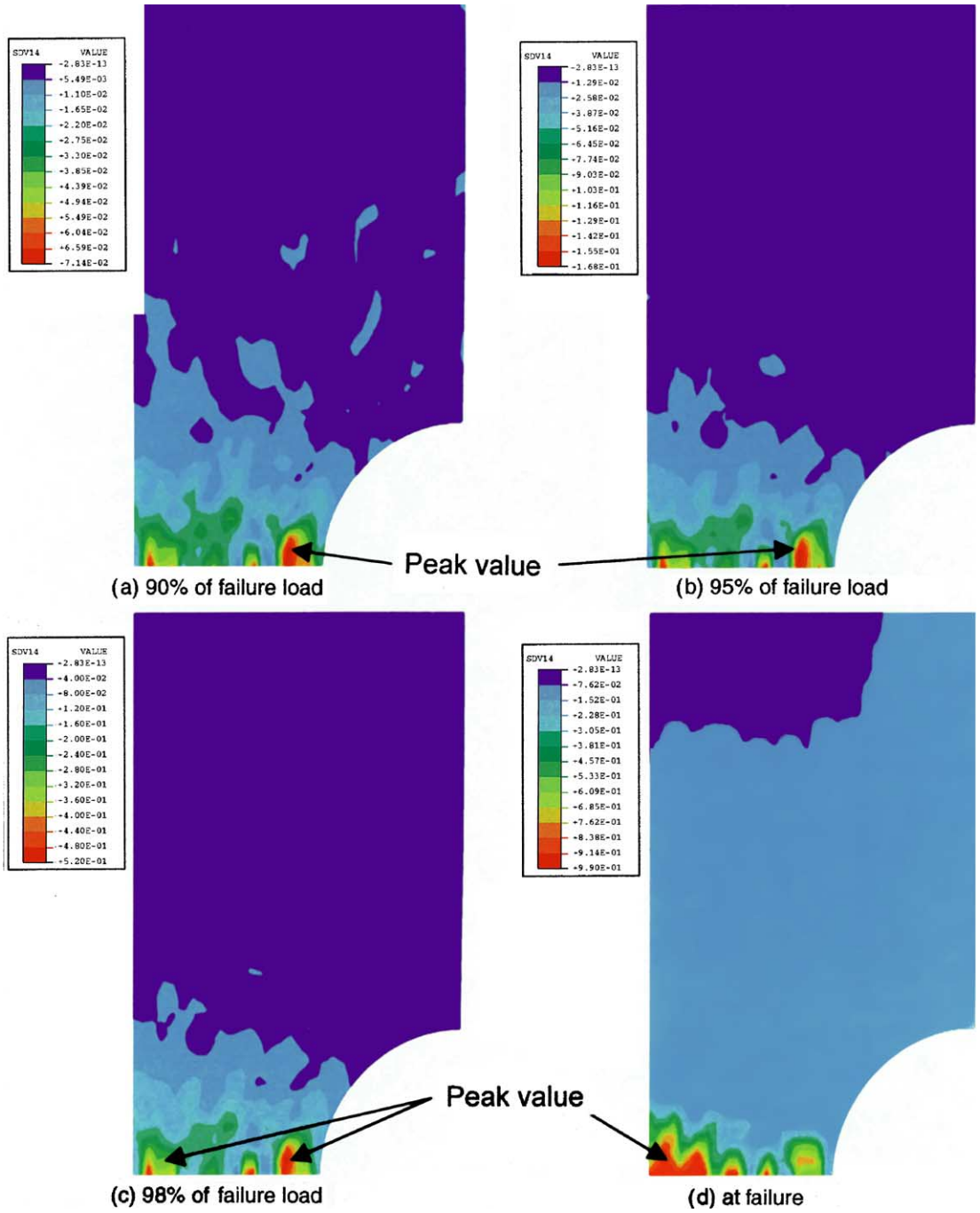

Fig. 9. Progression of damage, SDV14, in FEM simulations with initial random porosity level of 0.001.

because when the initial porosity level is small, total damage is not driven by casting pores but by voids nucleating from second phase particles. Although voids nucleate as a function of stress

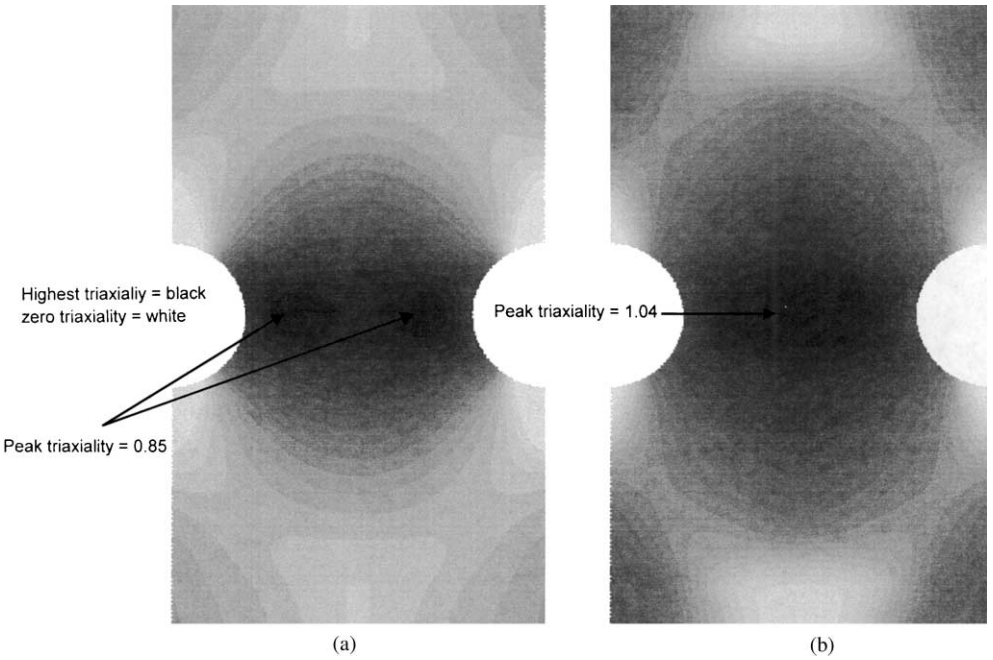

Fig. 10. Progression of stress triaxialities (hydrostatic stress/deviatoric stress) over the spatial domain of a notch specimen under tensile deformation.

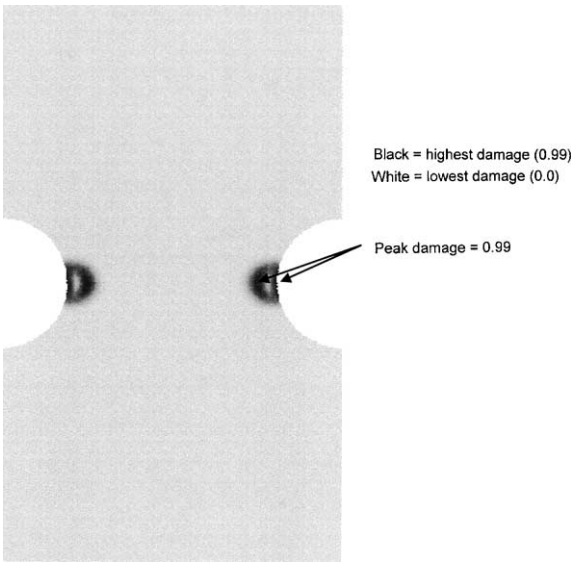

Fig. 11. Total damage contours just before final failure of a notch tensile specimen with a notch acuity to radius ratio of 0.117 for a cast A356 aluminum alloy. Note that the dark region indicates the peak damage level near the notch edge and between the center of the specimen and notch edge.

triaxiality their dependence on stress triaxiality is much less than for void growth. As such, the effective plastic strain, which is highest near the notch edge, drives the void nucleation and in this case the total damage. As the initial porosity level increases, damage from the second phase particles becomes less important compared to the void volume fraction of the casting pores. Hence, a mechanism change arises. When the casting pore volume fraction is high, the initial voids grow primarily as a function the stress triaxiality, which is highest at the specimen center. Fig. 9 illustrates that with an initial porosity level of 0.001 (and above), failure occurs at the specimen center as opposed to the notch edge. The work in [43] showed a similar trend for a wider range of initial porosity levels for wrought 6061-T6 aluminum, but no random initialization of porosity was performed in that study.

When comparing an initial random versus an initial homogeneous distribution of voids, it can be seen from Fig. 7 that different elongations at

failure arise, although the overall porosity level was the same in both cases. Just as different initial porosity level simulations were run with the homogeneous distribution, simulations with the same initial porosity levels were run with random distributions. The motive for analyzing the random case arises because the casting process can yield various pore sizes throughout the specimen. In all the cases, the random initialization always incurred a lower elongation at failure than did the homogeneous case. The effect of void size differences from neighbors is strong because the larger voids incur a larger plastic zone around the void thus enhancing void growth in neighboring small voids [38]. Though based upon these few simulations, the stress triaxiality from the notch seems to play more of a role than the effective plastic strain as both the low and high initial porosity levels tend to show failure towards the specimen center regardless of whether a random or homogeneous distribution exists.

The typical progression of damage evolution for wrought materials in notch tensile tests arises from voids growing at the center of the specimen because of the high stress triaxialities. Actually, the peak stress triaxiality starts at the notch edge at the start of the deformation because of the stress concentration but moves fairly rapidly to the center as deformation proceeds. The stress triaxiality is nonuniform throughout the cross-section of the specimen and reaches a level sufficient to start void growth when its peak value reaches the center of the notch specimen. Fig. 10 shows contour plots of the stress triaxiality (hydrostatic stress/deviatoric stress) of a notch tensile test illustrating spatial movement of the peak stress triaxiality. Again, this is typical for wrought, ductile materials that could even have a small fraction of brittle second phases.

For ductile materials with large scale brittle phases, such as the cast A356 aluminum alloy examined in this study, the final failure location may not occur at the specimen center depending on the fracture mechanisms of pore growth from casting porosity versus from silicon particle breakage. As the peak stress triaxiality increases in magnitude and moves toward the center of the specimen, voids have been nucleated by the fracture of the particles and/or by debonding of the particle–aluminum interface. As such, the damage increases

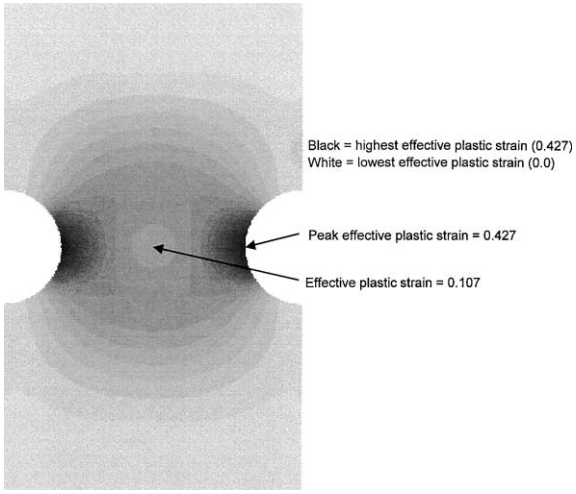

Fig. 12. Plastic strain contours just before final failure of a notch tensile specimen with a notch acuity to radius ratio of 0.117 for a cast A356 aluminum alloy. Note that the dark region indicates the peak plastic strain level near the notch edge.

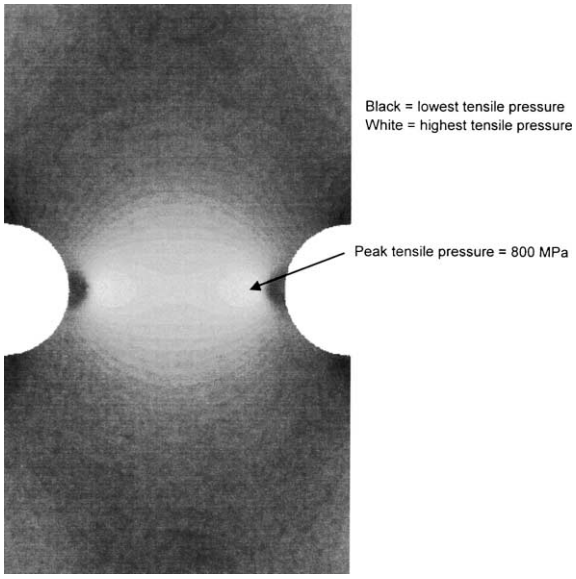

Fig. 13. Pressure contours just before final failure of a notch tensile specimen with a notch acuity to radius ratio of 0.117 for a cast A356 aluminum alloy. Note that the light region indicates the peak negative pressure (where the highest stress triaxiality occurs) between the center of the specimen and notch edge.

Table 2
Peak void volume fractions within notch specimen at different strain levels

Failure load (%)	X-ray tomography	FEM			
		($\phi_i = 0.0001$ homogeneous)	($\phi_i = 0.0001$ random)	($\phi_i = 0.001$ homogeneous)	($\phi_i = 0.001$ random)
90	0.028	0.003	0.056	0.069	0.071
95	0.186	0.017	0.124	0.155	0.168
98	0.451	0.123	0.445	0.483	0.520

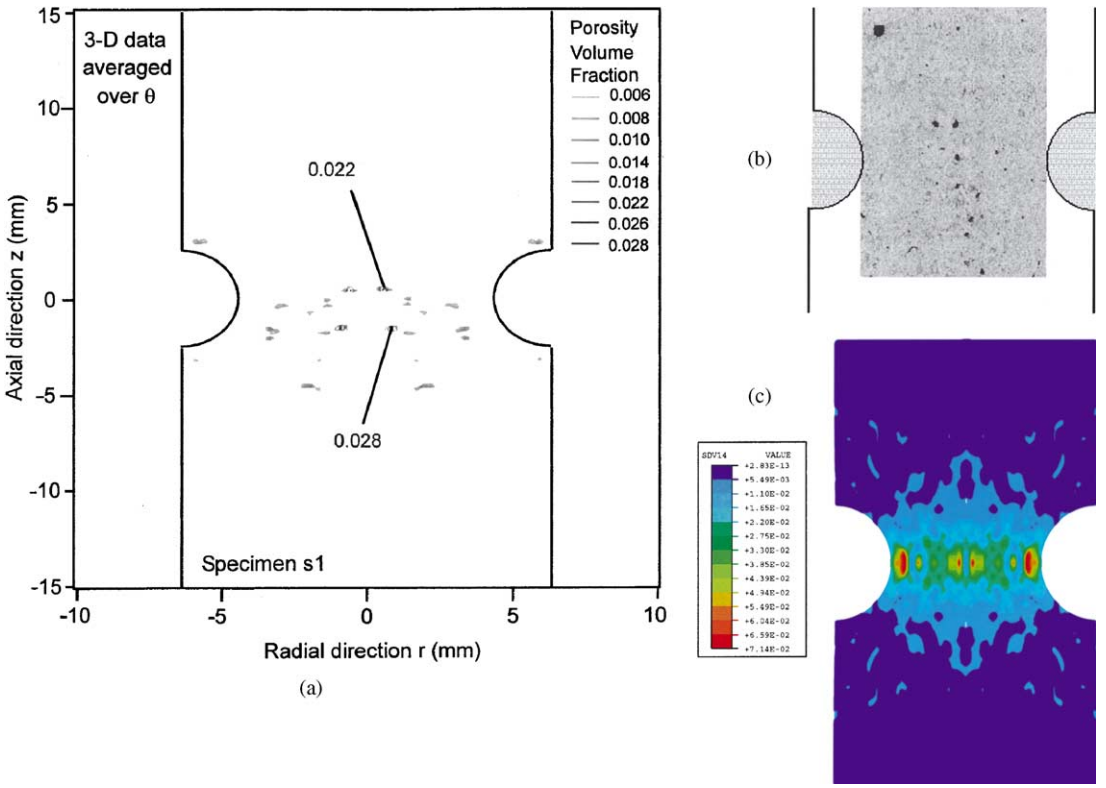

Fig. 14. Pictorial illustration of porosity distribution for the 90% of failure load specimen from (a) image analysis, (b) X-ray tomography, and (c) finite element simulation with an initially random distribution of porosity at a level of 0.001.

not only by voids growing but by new voids initiating and then growing as well. Damage reaches a critical level (interpreted as defining a hole in the material the size of the finite element) before it reaches the center of the specimen. In a wrought alloy at first element failure, the highest level of plastic strain occurs at the notch edge, but the highest stress triaxiality occurs at the center of the specimen. As such, we conclude that the stress triaxiality drives the void growth more than the plastic deformation, because damage evolves mainly at the specimen center. For this cast aluminum alloy, the highest plastic strain occurs at the notch edge and the stress triaxiality occurs away from the edge similar to wrought materials; however, Fig. 11 shows that the highest damage (which comprises void nucleation, growth, and coalescence) occurs at two different locations when

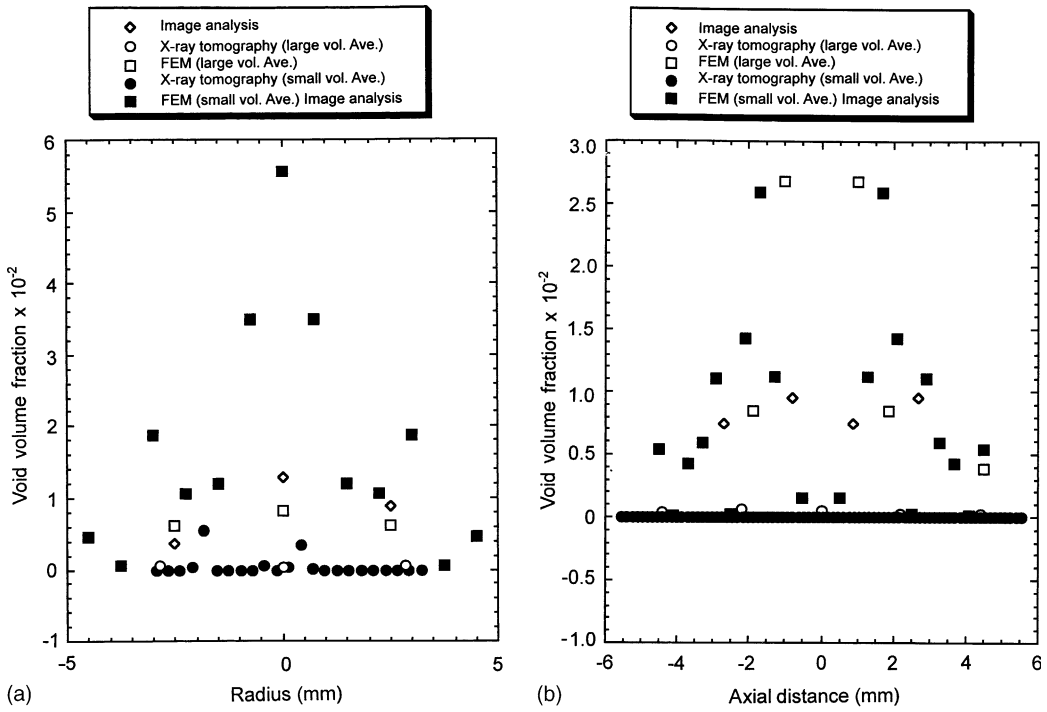

Fig. 15. Total void volume fraction determined for the 90% of failure load specimen from (a) image analysis, (b) X-ray tomography, and (c) finite element simulation with an initially random distribution of porosity at a level of 0.001.

the initially homogeneous distribution of porosity at 0.0001 was used. This low level of initial porosity allows for silicon particle damage to be a more dominant mechanism than void growth from casting porosity. The two different locations are aligned with the peak plastic strain and peak stress triaxiality as shown in Figs. 12 and 13, respectively. In Fig. 12, the dark contour shows that the plastic strain reached a level of 42% at the notch edge and around only 1% near specimen center. The highest negative tensile pressure shown in Fig. 13 (stress triaxiality equals the negative pressure over the deviatoric stress) occurs between the notch edge and specimen center. This is where the peak void growth occurs.

6. Results and discussion

The progression of damage in notch tensile specimens for this cast A356 aluminum alloy gives an understanding of the role of the nonhomogeneous distribution of initial porosity and second phase silicon on the final failure state. With this understanding, we now focus on comparisons of the finite element simulations and experimental results, which include image analysis and X-ray tomography of the physical specimens.

With a higher initial porosity level, pore growth and coalescence mechanism is more dominant than the void nucleation from the second phase material, albeit both interact together in the damage process. We summarize the FE simulation porosity levels in Table 2 with data from the X-ray tomography. The finite element results show that porosity levels comparable to the experimental results can be achieved by the right combination of initial porosity and distribution level. It appears that three of the cases could match the experimental data, but clearly the homogeneous distribution with an initial porosity of 0.0001 does not correlate well. Because different specimens were used in the tests with different initial porosity levels and amounts of randomness, comparison

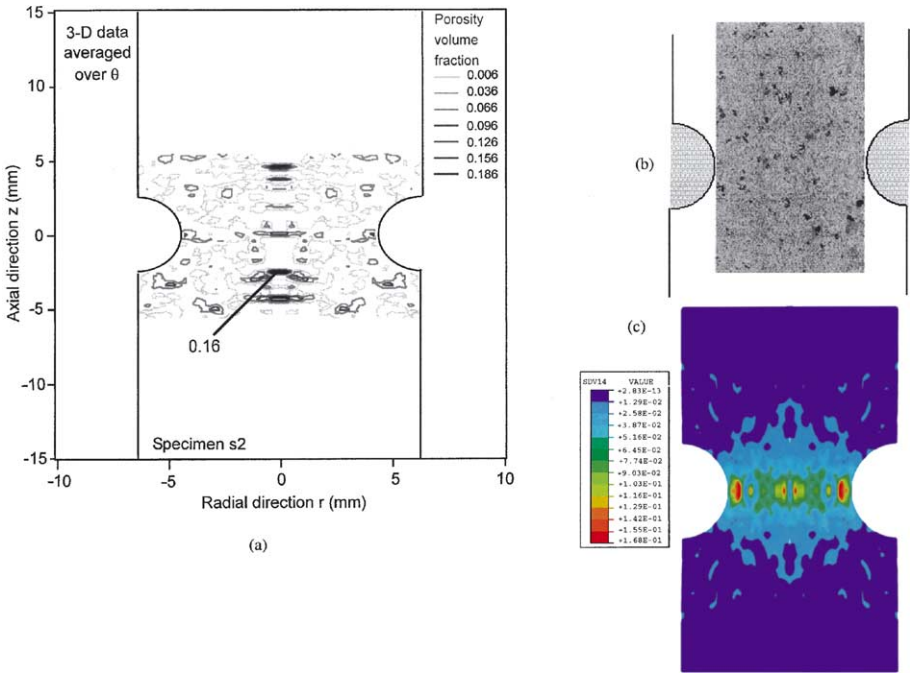

Fig. 16. Pictorial illustration of porosity distribution for the 95% of failure load specimen from (a) image analysis, (b) X-ray tomography, and (c) finite element simulation with an initially random distribution of porosity at a level of 0.001.

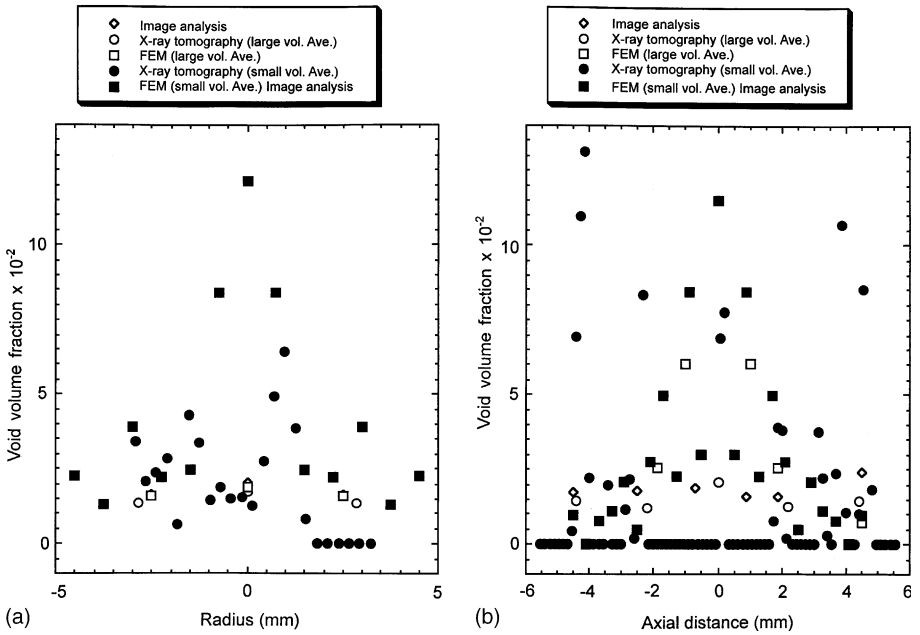

Fig. 17. Total void volume fraction determined for the 95% of failure load specimen from (a) image analysis, (b) X-ray tomography, and (c) finite element simulation with an initially random distribution of porosity at a level of 0.001.

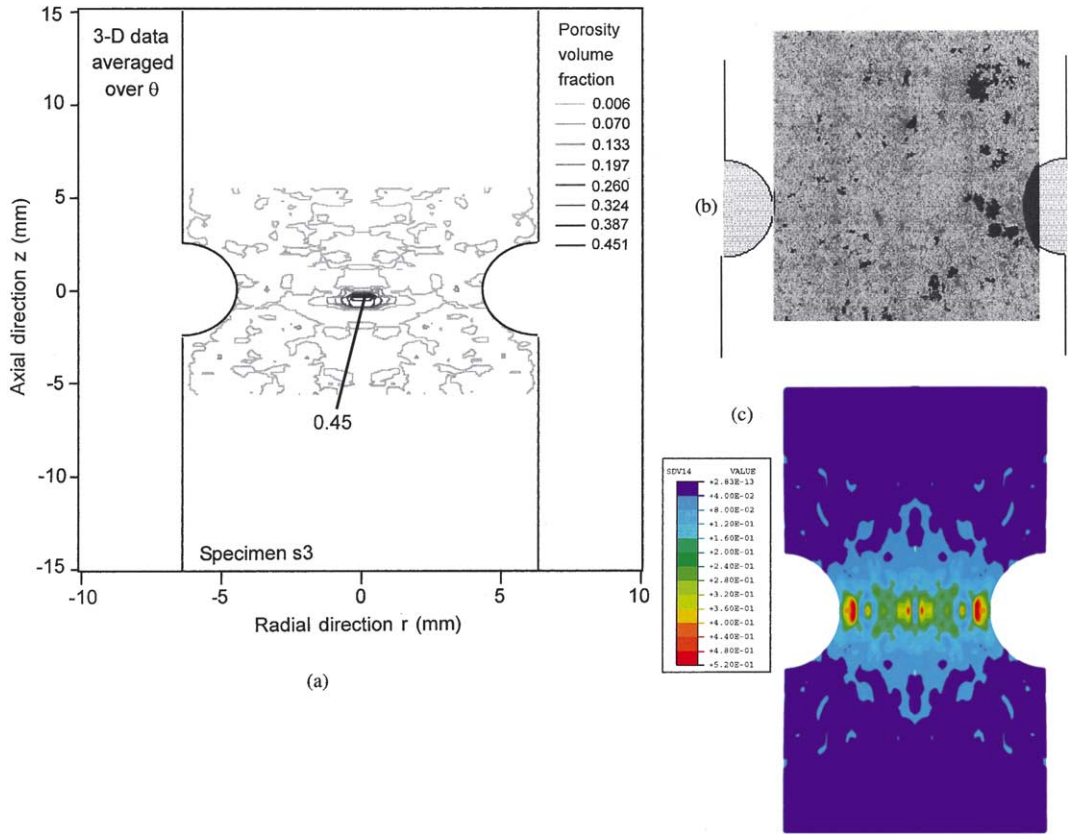

Fig. 18. Pictorial illustration of porosity distribution for the 98% of failure load specimen from (a) image analysis, (b) X-ray tomography, and (c) finite element simulation with an initially random distribution of porosity at a level of 0.001.

with FEM simulation comparisons show some differences. Clearly, the trends are similar, which suggests that the damage progression was driven more by the notch geometry and not the initial microstructure in this particular case although both certainly influence the final fracture.

Finite element and X-ray tomography results were not only determined over the highest spatial resolution, but comparisons to the image analysis results were considered by averaging over a larger region (three different sections).

Figs. 14–20 illustrate the comparisons for the small and large region averages. For Figs. 14, 16 and 18, high-resolution large area montages of the microstructure show the porosity distribution in the entire notch region of the specimens. The image analysis results were determined from a two-dimensional plane, and the finite element and X-ray results were taken circumferentially around the axisymmetric geometry. Although three-dimensional porosity levels can be approximated by two-dimensional image analysis measurements [61], the X-ray tomography and finite element analyses results were typically closer. This can be seen clearly in Fig. 18. Recall that the image analysis resolution was 0.5 μm and the X-ray resolution was 28 μm. Almost an order of magnitude higher. As such, the lower scale shrinkage below 28 μm was not captured by the X-ray tomography results.

Fig. 18 shows a comparison of the image analysis montage, X-ray tomography picture, and a contour plot of total void volume fraction from the finite element simulation in which an initially random porosity level of 0.001 was assumed for the 90% of fracture load case. The differences in

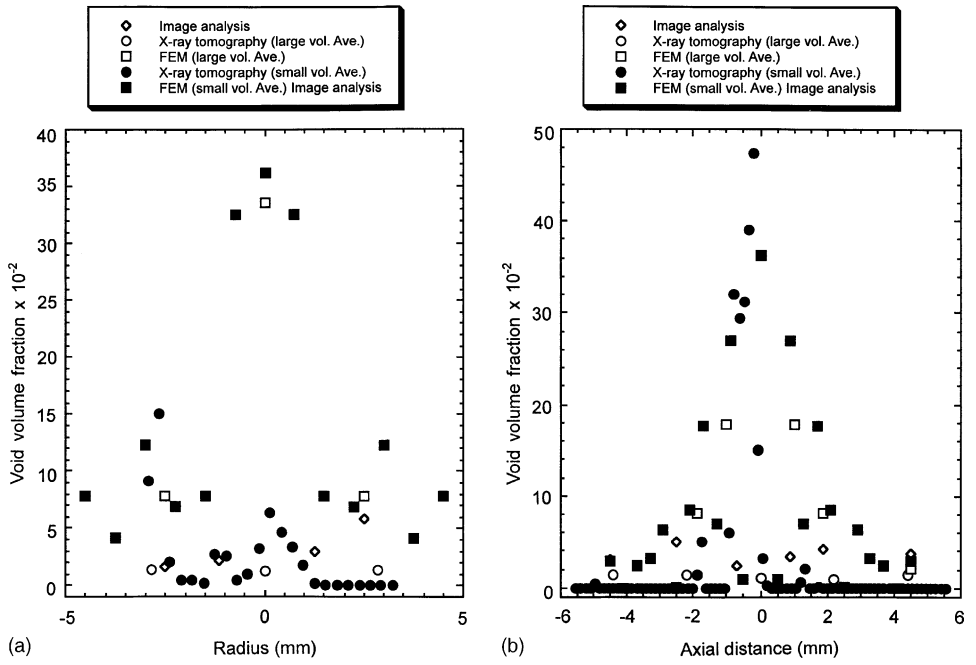

Fig. 19. Total void volume fraction determined for the 98% of failure load specimen from (a) image analysis, (b) X-ray tomography, and (c) finite element simulation with an initially random distribution of porosity at a level of 0.001.

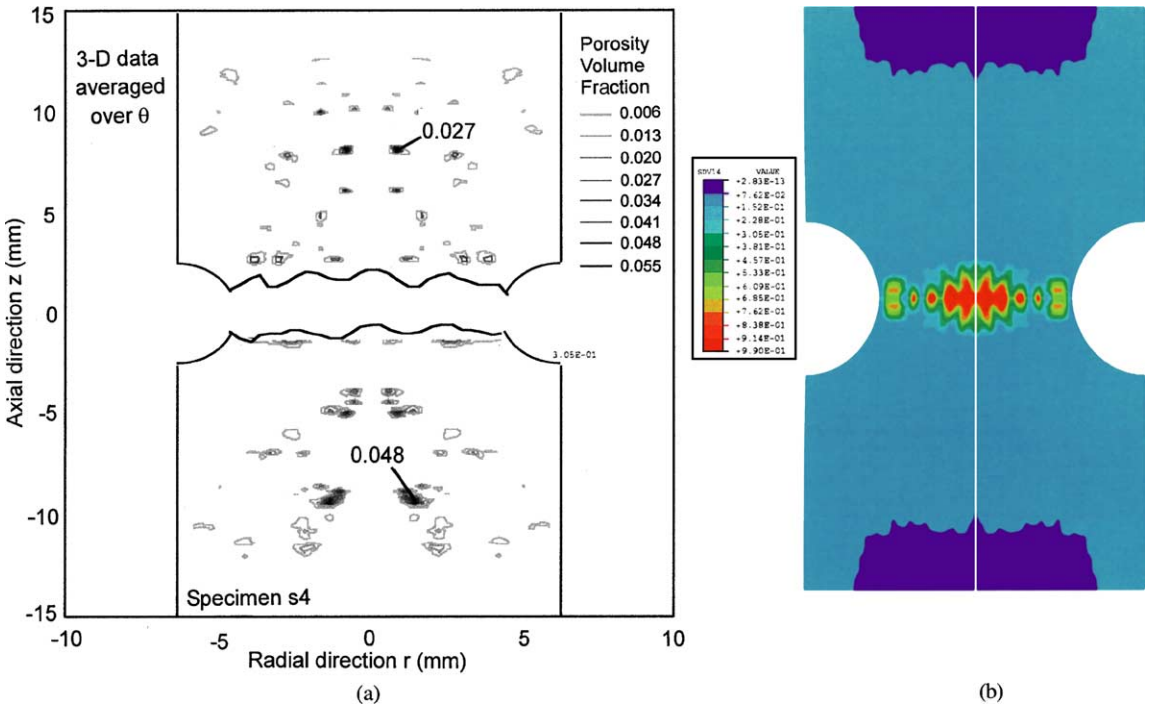

Fig. 20. X-ray tomography data of fractured specimen illustrating the final porosity level.

the montage and X-ray tomography picture arise because the image analysis only shows one plane cutting axially through the specimen. The X-ray tomography results average 360 planes rotated at one degree throughout the specimen. As one would expect, the X-ray tomography results slightly differ than the image analysis results but closer the finite element analysis, since the same axisymmetric assumptions are included in the simulations. Although the peak values are different between the X-ray tomography and finite element simulations, the maximum void volume fraction is largest at $z = 0$ in the axial direction for both and decreases as the direction z increases or decreases.

Fig. 15 is the quantitative data retrieved from Fig. 14. When comparing the X-ray tomography and FEM results, one can see that the FEM peak void volume fraction (total damage) is slightly higher (7.1–2.8%). The difference peak void volume fraction arises due to the initial porosity level assumption. However, the general character and distribution seems to match fairly well. The reader should keep in mind when comparing the finite element simulations with the X-ray results that the resolution is finer for the simulations and a lower bound cut-off exists for the X-ray results. Given these constraints, the comparisons are encouraging.

Comparisons along both the radius and axial dimensions were made within the specimens. Since the notch induces a stress triaxiality that drives void growth from the specimen center, one can observe a higher void volume fraction at the center than at the edge. Figs. 14–20 confirm this notion.

Figs. 16 and 17 showed similar qualitative trends as Figs. 14 and 15 but for the 95% of failure load case. Here, the porosity levels are higher than the 90% case (Figs. 14 and 15) as damage has progressed, and all three methods (X-ray tomography, optical metallography, and finite element analysis) quantitatively capture the trend fairly well.

Figs. 18 and 19 show the comparisons for the 98% of fracture load case. Fig. 20 shows a specimen that was fractured in the center and the correlating finite element simulation comparison showing the fracture at the center as well. Again, all three methods appear to reflect the expected damage progression.

Based on these six figures, one's confidence in all three methods is enhanced since they seem to independently corroborate each other's results in terms of maximum void volume levels and their correlating distributions. Minor differences in the X-ray tomography and optical image results arise because each of the measurements were from different specimens which had different initial porosity levels, while the finite element simulations were from a single calculation using an initial starting porosity level of 0.001 that provided qualitative damage progression agreement with both the X-ray tomography and optical metallography. Interestingly, on a particular wrought 304L stainless steel [62] different initial porosity levels experimentally still gave final failure starting at the notch center. For these castings, final failure may or may not start there depending on the initial void volume fraction and void distribution.

7. Conclusions

Damage progression has been quantified and confirmed by independent methods of evaluation for a cast A356 aluminum alloy notch tensile testing. The methods include experiments; X-ray CT; optical microscopy/stereology metallography image analysis; and finite element simulations that include a history dependent elastic–plastic ISV plasticity model involving evolution equations for void nucleation, growth, and coalescence. Furthermore, parametric finite element simulations were performed to give insight into various initial conditions and responses of the notch tensile bars. This study provides a new methodology of evaluating metal damage progression and provides the quantitative data needed to establish increased confidence in using a simulation-based finite element analysis to achieve optimal geometries and reduced masses for structural components.

Acknowledgements

The work by M.F. Horstemeyer and Ken Gall was performed at the US Department of Energy

Sandia National Laboratories under contract DE-AC04-94AL85000. The work of K.W. Dolan, J.J. Haskins, and D.E. Perkins was performed under the at the US Department of Energy Lawrence Livermore National Laboratory under contract W-7405-Eng-48. Richard Osborne, Gerry Shulke, Don Penrod, and Westmoreland Mechanical Testing and Research are to be thanked for their roles in performing this work.

Appendix A. Material model constants

Constant	Value	Constant	Value
C_1 (MPa)	53.09	C_{16} (MPa/K)	4.622
C_2 (K)	945.3	C_{17} ($MPa^{-1}\,s^{-1}$)	0
C_3 (MPa)	155.9	C_{18} (K)	0
C_4 (K)	110.5	C_{19}	0
C_5 (s^{-1})	10^{-5}	C_{20}	0
C_6 (K)	0	C_{21}	−5
C_7 (MPa^{-1})	1.128e−3	C_{22}	−0.3895
C_8 (K)	−1796	a (MPa)	615,460
C_9 (MPa)	4820	b (MPa)	58,640
C_{10} (MPa/K)	10.94	c (MPa)	30,011
C_{11} ($MPa^{-1}\,s^{-1}$)	2.385e−3	K_{IC} ($MPa\,mm^{0.5}$)	17.3
C_{12} (K)	1441	d (μm)	4e−6
C_{13} (MPa^{-1})	1.674e−3	f	0.07
C_{14} (K)	0	C_{coal}	0.23
C_{15} (MPa)	2818		

References

[1] W.M. Garrison, N.R. Moody, Ductile fracture, J. Phys. Chem. Solids 48 (1987) 1035–1074.
[2] I.G. Palmer, G.C. Smith, Fracture of internally oxidized copper alloys, in: Proc. AIME Conf. Oxide Dispersion Strengthening, Bolton Landing, NY, Gordon and Breach, NY, 1967.
[3] J. Gurland, Observations on the fracture of cementite particles in a spheodized 1.05% C steel deformed at room temperature, Acta Metall. 20 (1972) 735–741.
[4] T.B. Cox, J.R. Low, An investigation of the plastic fracture of AISI 4340 and 18 Nickel-200 grade maraging steels, Metall. Trans. 5A (1974) 1457–1470.
[5] G.T. Hahn, A.R. Rosenfield, Metallurgical factors affecting fracture toughness of aluminum alloys, Metall. Trans. 6A (1975) 653–668.
[6] E.N. Pan, C.S. Lin, C.R. Lopez, Effects of solidification parameters on the feeding efficiency of A356 aluminum alloy, AFS Trans. 98 (1990) 735–746.
[7] E.N. Pan, H.S. Chiou, G.J. Liao, Effects of modification and solidification conditions on the feeding behavior of A356 Al alloy, AFS Trans. 99 (1991) 605–621.
[8] A.M. Samuel, F.H. Samuel, A metallographic study of porosity and fracture behavior in relation to the tensile properties in 319.2 end chill castings, Metall. Trans. 26A (1995) 2359–2372.
[9] M.F. Horstemeyer, S. Ramaswamy, On factors affecting localization and void growth in ductile metals: A parametric study, Int. J. Damage Mech. 9 (2000) 5–28.
[10] R.C. Harris, S. Lipson, H. Rosenthal, Tensile properties of aluminum–silicon magnesium alloys and the effect of sodium modification, AFS Trans. 64 (1956) 470–481.
[11] S.F. Frederick, W.A. Bailey, The relation of ductility to dendrite cell size in a cast Al–Si–Mg alloy, Trans. Metall. Soc. AIME 242 (1968) 2063–2067.
[12] O. Vorren, J.E. Evensen, T.B. Pedersen, Microstructure and mechanical properties of AlSi(Mg) casting alloys, AFS Trans. 92 (1984) 459–466.
[13] J.W. Yeh, W.P. Liu, The cracking mechanism of silicon particles in an A357 aluminum alloy, Metall. Mater. Trans. 27A (1996) 3558–3568.
[14] C.H. Caceres, C.J. Davidson, J.R. Griffiths, The deformation and fracture behavior of an Al–Si–Mg casting alloy, Mat. Sci. Eng. A 197 (1995) 171–179.
[15] B. Closset, J.E. Gruzleski, Mechanical properties of A356.0 alloys modified with pure strontium, AFS Trans. 90 (1982) 453–464.
[16] J. Gurland, J. Plateau, The mechanism of ductile rupture of metals containing inclusions, Trans. ASM 56 (1963) 442.
[17] M.F. Ashby, Work hardening of dispersion-hardened crystals, Phil. Mag. 14 (1966) 1157–1178.
[18] A.R. Rosenfield, Criteria for ductile fracture of two-phase alloys, Metall. Rev. 13 (1969) 29–40.
[19] F.A. McClintock, A criterion for ductile fracture by the growth of holes, J. Appl. Mech. 35 (1968) 363–371.
[20] J.R. Rice, D.M. Tracey, On the ductile enlargement of voids in triaxial stress fields, J. Mech. Phys. Solids 17 (1969) 201.
[21] T.W. Barbee, L. Seaman, R. Crewdson, D. Curran, Dynamic fracture criteria for ductile and brittle metals, J. Mater. JMLSA 7 (1972) 393–401.
[22] A.S. Argon, J. Im, Safoglu, Cavity formation from inclusions in ductile fracture, Metall. Trans. 6A (1975) 825–837.
[23] R. Raj, M.F. Ashby, Intergranular fracture at elevated temperature, Acta Metall. Mater. 23 (1975) 653.
[24] A.L. Gurson, Continuum theory of ductile rupture by void nucleation and growth. 1. Yield criteria a and flow rules

for porous ductile media, J. Engng. Mater. Tech. 99 (1977) 2–15.
[25] A. Needleman, J.R. Rice, Limits to ductility set by plastic flow localization, in: Koistinen, Wang (Eds.), Mechanical Sheet Metal Form, Plenum Publishing Co., 1978, pp. 237–265.
[26] S.H. Goods, L.M. Brown, The nucleation of cavities by plastic deformation, Acta Metall. 27 (1979) 1–15.
[27] M. Saje, J. Pan, A. Needleman, Void nucleation effects on shear localization in porous plastic solids, Int. J. Fract. 19 (1982) 163–182.
[28] J.P. Hirth, W.D. Nix, Analysis of cavity nucleation in solids subjected to external and internal stresses, Acta Metall. Mater. 33 (1985) 359.
[29] V. Tvergaard, Ductile fracture by cavity nucleation between larger voids, J. Mech. Phys. Solids 30 (1982a) 265–286.
[30] V. Tvergaard, On localization in ductile materials containing spherical voids, Int. J. Fract. 18 (1982b) 237–252.
[31] V. Tvergaard, Material failure by void coalescence, Adv. Appl. Mech. 27 (1990) 83–151.
[32] A. Needleman, A continuum model for void nucleation by inclusion debonding, J. Appl. Mech. 54 (1987) 525–531.
[33] C.L. Hom, R.M. McMeeking, Void growth in elastic–plastic materials, J. Appl. Mech. 56 (1989) 309–317.
[34] D.J. Bammann, E.C. Aifantis, A damage model for ductile metals, Nucl. Eng. Des. 116 (1989) 355–362.
[35] A.C.F. Cocks, Inelastic deformation of porous materials, J. Mech. Phys. Solids 37 (1989) 693–715.
[36] P.P. Castaneda, M. Zaidman, Constitutive models for porous materials with evolving microstructure, J. Mech. Phys. Solids 42 (1994) 1459–1497.
[37] M.F. Horstemeyer, A.M. Gokhale, A void-crack nucleation model for ductile metals, Int. J. Solids Struct. 36 (1999) 5029–5055.
[38] M.F. Horstemeyer, M.M Matalanis, A.M. Sieber, M.L. Botos, Micromechanical finite element calculations of temperature and void configuration effects on void growth and coalescence, Int. J. Plast. (2000) 16.
[39] A. Seweryn, Z. Mroz, On the criterion of damage evolution for variable multiaxial stress states, Int. J. Solids Struct. 35 (1998) 1589–1616.
[40] A. Tewari, M. Dighe, A.M. Gokhale, Quantitative characterization of spatial arrangement of micropores in cast microstructures, Mat. Char. 40 (1998) 119–132.
[41] D.J. Bammann, M.L. Chiesa, M.F. Horstemeyer, L.I. Weingarten, Failure in ductile materials using finite element methods, in: N. Jones, T. Weirzbicki (Eds.), Structural Chrashworthness and Failure, Elsevier Applied Science, 1993.
[42] D.J. Bammann, M.L. Chiesa, G.C. Johnson, Modeling large deformation and failure in manufacturing processes, in: Tatsumi, Wannabe, Kambe (Eds.), Theor. Appl. Mech., Elsevier Science, 1996, pp. 259–276.
[43] M.F. Horstemeyer, J. Lathrop, A.M. Gokhale, M. Dighe, Modeling stress state dependent damage evolution in a cast Al–Si–Mg aluminum alloy, Theor. Appl. Fract. Mech. 33 (2000) 31–47.
[44] M.F. Horstemeyer, V. Revelli, Stress history dependent localization and failure using continuum damage mechanics concepts, in: Applications of Continuum Damage Mechanics to Fatigue and Fracture, ASTM STP 1315, ASTM, 1997, pp. 216–237.
[45] P. Louis, A.M. Gokhale, Application of image analysis for characterization of spatial arrangement of features in microstructures, Metall. Mater. Trans. 26A (1995) 1449–1456.
[46] P. Louis, A.M. Gokhale, Computer simulation of spatial arrangement and connectivity of particles in three dimensional microstructure: Application to model electrical conductivity of polymer matrix composite, Acta Metall. Mater. 44 (1996) 1519–1528.
[47] S. Yang, A. Tewari, A.M. Gokhale, Modelling of non-uniform spatial arrangement of fibers in a ceramic matrix composite, Acta Mater. 45 (1997) 3059–3069.
[48] J.R. Rice, Inelastic constitutive relations for solids: An internal variable theory and its application to metal plasticity, J. Mech. Phys. Solids 9 (1971) 433–455.
[49] M.P. Miller, D.L. McDowell, Stress state dependence of finite strain inelasticity, in: ASME Summer Mechanics Meeting, Tucson, AZ, ASME-AMD, 32, Microstructural Characterization in Constitutive Modeling of Metals and Granular Media, 1992, pp. 27–44.
[50] M.P. Miller, P.R. Dawson, D.J. Bammann, Reflecting microstructrual evolution in hardening models for polycrystalline metals, in: Shen, Dawson (Eds.), Simulation of Materials Processing: Theory, Methods, and Applications, Balkema, Rotterdam, 1995.
[51] M.F. Horstemeyer, D.L. McDowell, D.J. Bammann, Torsional softening and the forming limit diagram, in: K. Chen (Ed.), SAE Tech. Ser. 960599, Analysis of Autobody Stamping Technology, 1995.
[52] M.L. Kachanov, Time of the fractured process under creep conditions, Izv. Akad. Nauk. SSSR OTN Tekh. Nauk. 8 (1958) 26.
[53] Y.N. Rabotnov, Creep Problems in Structural Members, North-Holland, Amsterdam, 1969.
[54] A.K. Miller, Unified approach to predicting interactions among creep, cyclic plasticity, and recovery, Nucl. Eng. Des. 51 (1) (1978) 35–43.
[55] R. DeBorst, Smeared cracking, plasticity, creep, and thermal loading: A unified approach, Comput. Meth. Appl. Mech. Eng. 62 (1987) 89–110.
[56] M.F. Horstemeyer, Damage of HY100 steel plates from oblique constrained blast waves, in: J.H. Giovanola, A.J. Rosakis (Eds.), Advances in Local Fracture/Damage Models for the Analysis of Engineering Problems, Book No. H00741, vol. AMD 137, 1992.
[57] M.F. Horstemeyer, Structural analysis of a submarine using statistical design of experiments, in: E.P. Chen, V.K. Luk (Eds.), Advances in Numerical Simulation Techniques for Penetration and Perforation of Solids, ASME Winter Meeting, vol. AMD 171, 1993.

[58] A.C.F. Cocks, M.F. Ashby, On creep fracture by void growth, Prog. Mater. Sci. 27 (1982) 189–244.
[59] M.F. Horstemeyer, A numerical parametric investigation of localization and forming limits, Int. J. Damage Mech. 9 (2000) 255–285.
[60] B. Budiansky, J.W. Hutchinson, S. Slutsky, Void growth and collapse in viscous solids, in: H.G. Hopkins, M.J. Sewell (Eds.), Mechanics of Solids, Pergamon Press, Oxford, 1982, pp. 13–45.
[61] E.E. Underwood, Quantitative Stereology, Edison-Wesley, Reading Mass, 1970.
[62] W.Y. Lu, M.F. Horstemeyer, J. Korellis, R. Grishibar, D. Mosher, High temperature effects in 304L stainless steel notch tests, Theor. Appl. Fract. Mech. 30 (1998) 139–152.